33RD CONGRESS
OF THE INTERNATIONAL COUNCIL
OF THE AERONAUTICAL SCIENCES
STOCKHOLM, SWEDEN, 4-9 SEPTEMBER, 2022

ICAS 2022 SWEDEN

XRF1 HIGH-LIFT LOAD ANALYSIS OF WING AND HIGH-LIFT SYSTEM

Sven Pülm[1], Vega Handojo[2] & Ruben B. Seidler[1]

[1]DLR - Institute of Aerodynamics and Flow Technology, Dep. Transport Aircraft,
Lilienthalplatz 7, 38108 Braunschweig, Germany
e-mail: sven.puelm@dlr.de & ruben.seidler@dlr.de
[2]DLR - Institute of Aeroelasticity, Dep. Loads Analysis and Aeroelastic Design,
Bunsenstr. 10, 37073 Göttingen, Germany
e-mail: vega.handojo@dlr.de

Abstract

To investigate the potential of wing load alleviation in cruise flight, the repercussions on take-off, approach and landing are of high interest for an extensive evaluation. By considering the CS-25 regulations of EASA, relevant load cases for certification were worked out. Computational fluid dynamics (CFD) analysis of the Airbus XRF1 research testcase in high-lift configuration were performed to obtain aerodynamic information on loads on wing and high-lift devices. Using a condensed structural model, the aerodynamic loads are superposed with the inertial loads, so that cut loads on the load reference axis as well as component loads on the slats and flaps can be derived.

Keywords: load alleviation, XRF1, high-lift, loads, devices

1. Introduction

In search of more potential for efficiency improvement of transport aircrafts new concepts and technologies are developed. One of these approaches are the application of passive (e.g. adapted stiffness of structures by aeroelastic tailoring) and active load alleviation (e.g. deflection of flaps and rudders for redistribution of aerodynamic loads during maneuvers or alleviation of gust loads). These technologies allow to reduce the mass of the wing structure, which further on reduces fuel consumption. The reduced wing weight also makes it more attractive to further implement technologies like natural laminar flow wings for drag reduction, which usually increase wing weight. By applying a combination of maneuver and gust load alleviation techniques on a turbulent wing Xu and Kroo [1] decreased the wing weight by 12.1 %. This lead to a fuel burn reduction of 11.2 % and a cost reduction of 7.3 %. Furthermore, they also incorporated natural laminar flow investigations and improved the fuel burn and cost reduction to 18.4 % and 11 %, respectively. Binder et al. [2] combined active load alleviation (maneuver and gust) with aeroelastic tailoring to investigate the interactions of these techniques on each other on a transport aircraft with conventional control surface layout. Both references emphasize that the combination of these technologies is the key to exploit most of the potential. As a next step to minimize costs even further, Handojo [3] investigated active and passive load alleviation in a pre-design process to utilize these advantages in an early aircraft design phase. All these efforts were also addressed in the project Con.Move/NEKON [4] and are followed up in the project In-Fly-Tec/APLAUS, funded by the German Ministry for Economic Affairs and Climate Action within the "Luftfahrtforschungsprogramm", in which the work described below is settled.

Until now, the cruise flight loads are usually the basis for structural optimization and thus determine the wing mass. However, the question arises whether the loads in high-lift conditions become dominant for wing sizing when maneuver and gust load alleviation methods for cruise flight are integrated. If this is the case, the high-lift load requirements would diminish the newly gained potential. To investigate this eventuality, the high-lift system of the XRF1, which was designed in Con.Move, is used.

The presented approach includes computational fluid dynamics (CFD) calculations with steady Reynolds-Average Navier-Stokes (RANS) equations of several high-lift load cases prescribed by the certification specifications of the European Union Aviation Safety Agency (EASA's CS-25) [5]. A post-process merges the resulting aerodynamic load data with a simplified structural model including masses to cut loads. Further analysis are shown for the aerodynamic loads on the high-lift devices.

2. Aicraft Description & References

2.1 XRF1 aircraft

The XRF1 (eXternal Research Forum) is an Airbus provided industrial standard multi-disciplinary research testcase representing a typical configuration for a long-range wide-body aircraft. This research testcase is used by Airbus to engage with external partners on development and demonstration of relevant capabilities and technologies. It has already been used in several projects e.g. for investigating the effect of a winglet with tab deflection on wing loads [6], designing a reference composite wing including gust, maneuver and landing loads [7] for further Multi Disciplinary Optimizations (MDO) or for detailed MDO in the DLR (German Aerospace Center) project VicToria [8]. The provided aircraft data includes geometric definitions like CAD (computer aided design) models (s. Figure 1), structural and mass models and top level aircraft requirements (TLARs).

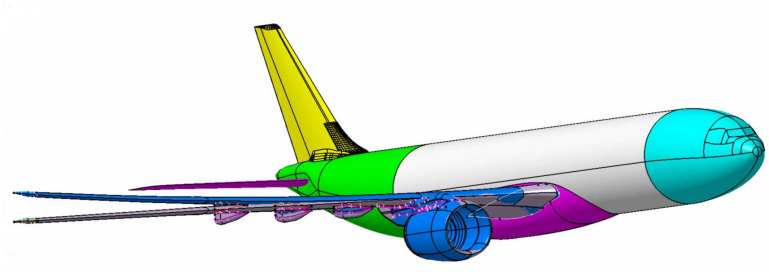

Figure 1 – XRF1 long-range wide-body aircraft

2.2 High-Lift System Design

In order to deepen the understanding of low speed aerodynamics on state-of-the-art passenger aircrafts, the DLR designed a high-lift system for the Airbus XRF1 research aircraft. Up to this point the aircraft model consisted of a clean geometric shape for cruise conditions, with a nacelle but without a high-lift geometry. Therefore the DLR developed the outlines of the movables on the wing and implemented the geometry of a fully extendable high-lift system, consisting of a trailing edge flap, a leading edge slat, the aileron and the flap track fairings. In Figure 2 a full view of the XRF1 high-lift geometry in its landing configuration is shown. The different movables are highlighted in different colors, blue for the flaps, red for the slats, grey for the aileron and black for the flap track fairings. In the top-right corner the inboard slat near the nacelle is depicted, in the bottom-right corner the movable flap track fairings are highlighted. Every component is fully movable with its own angle parameter, from a retracted position for cruise conditions to a fully extended configuration for landing.

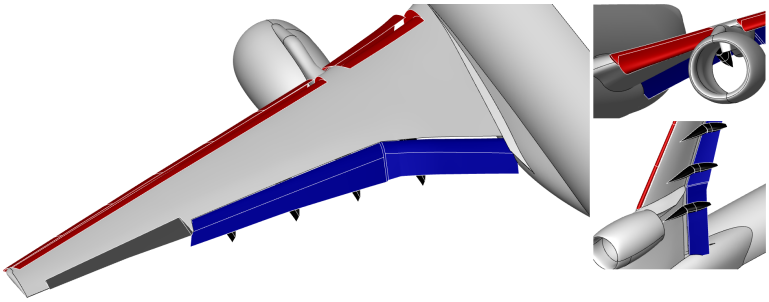

Figure 2 – XRF1 high-lift design in landing configuration, new implemented movables are highlighted as flaps (blue), slats (red), aileron (grey) and flap track fairings (black)

The trailing edge consists of an inboard and an outboard flap, which extend about two thirds of the wingspan of the XRF1 in spanwise direction. In chordwise direction the trailing edge consists of 15% of the chord length for the inboard flap, and due to the tapering of the wing it rises up to 25% chord length at the outboard flap. The spanwise change of flap movement due to the different motion paths causes a gap change at the outboard edge of the outboard flap. To compensate this behavior an oblique flap side was introduced. The flaps are mounted on a fixed bearing at the inboard support and floating bearings on the middle and outboard support.
The slat is designed over the complete leading edge of the wing, with a cut-out at the intersection with the overlapping pylon position of the nacelle. A wide gap is hereby prevented due to a slat motion normal to the front spar and tilted slat sides ensure small side edge gaps. The chordwise gap size is thereby achieved to be as small as possible. The outboard slat is segmented and consists of six elements, numerated from 2, next to pylon, to 7, at wingtip.
In Table 1 the possible XRF1 high-lift configurations for the low-speed cases are listed. The positions

Table 1 – Nominal slat, flap and aileron angles in degree for low-speed configurations

Configuration Name	CLEAN	1	1+F	2	3	FULL
	Cruise	Take-off			Take-off/Approach	Landing
Leading Edge						
Slat deflection (all)	0	15	15	22	22	22
sealed/vented	sealed	vented	vented	vented	vented	vented
Trailing Edge						
Flap deflection (all)	0	0	10	20	28	33
Aileron droop	0	5	5	10	10	10

are segmented into cruise, take-off and landing configuration and subdivided by the angle positions of all slats, all flaps and the aileron. All deflected slat positions have a vented gap. With the intention for a first analysis and quantification of the characteristics of the XRF1 high-lift system, detailed CFD studies were conducted on the take-off and landing configurations. The aerodynamic parameters were set to simulate start and landing with a Mach number of 0.2, a Reynolds number of $35 \cdot 10^6$ and ground conditions. Since the XRF1 did not have an existing horizontal tail plane (HTP) at this time, the results here are published without the influence of the aerodynamics of the HTP, but with lift coefficients compensating trim forces. In Figure 3 and 4 the results for configuration 1+F, 2, 3 and Full are shown.
Figure 3 hereby shows the lift coefficient C_L over the angle of attack α of the aircraft for the four different configurations. In general it can be seen, that the first draft of the XRF1 high-lift system shows a very good aerodynamic behavior, especially for take-off configuration 3 and landing configuration with a fully extended slat at 22 deg. Both configurations have a steady rise in lift coefficient with increasing angle of attack up to their maximum lift with no noticeable lift declines. Figure 4 shows the same lift coefficient now in relation to the correlating drag coefficient C_D. Here it can be seen, that the take-off 1+F has a strong increase in drag when reaching the non-linear lift region. The more retracted slats lead to a stronger sealing of the gaps between pylon and leading edge and amplify a vortex, which leads to a sharp flow separation on the upper surface of the wing, directly behind the cut-out section of the leading edge behind the pylon. In order to improve the aerodynamic behavior of the high-lift system for these configurations, it is planned to add strakes on the nacelle of the XRF1 to influence the vortex formation and direction for the final design.

2.3 Structural model and load reference axis

The structural and mass model, which is used to evaluate the high-lift loads, is the XRF1-DLR-C that is described by Handojo et al. [9] and denoted as the turbulent variant in that paper. The structure of the lifting surfaces is modelled with shell elements and the fuselage is represented by beam elements. In addition, finite element (FE) models of the control surfaces are generated and

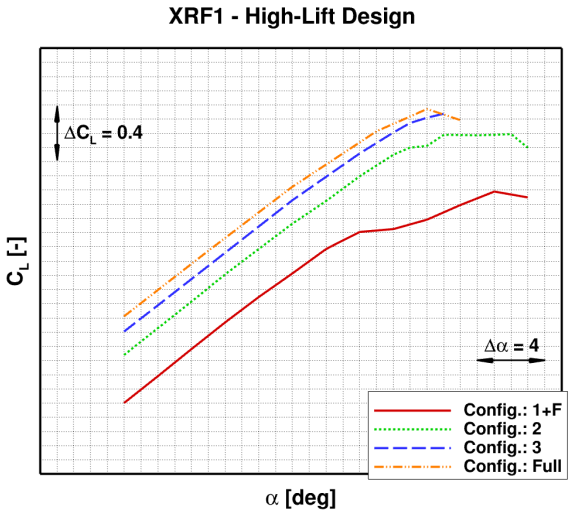

Figure 3 – XRF1 high-lift design: static CFD simulation results: C_L over α

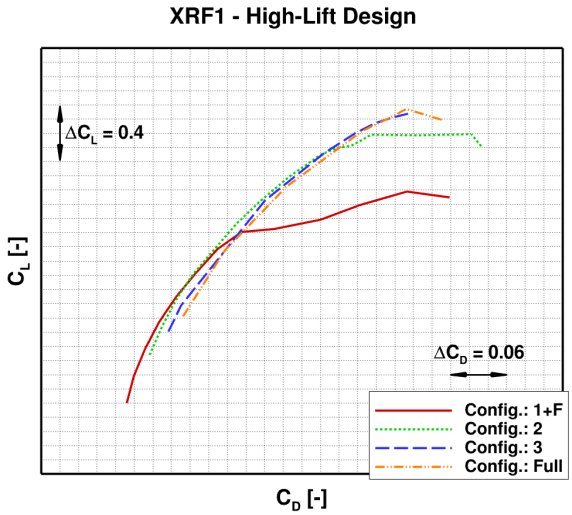

Figure 4 – XRF1 high-lift design: static CFD simulation results: C_L over C_D

connected to the primary structure using massless bar elements. Figure 5 visualizes the FE model of the XRF1-DLR-C. The shell elements on the engine nacelles are for visualization only.

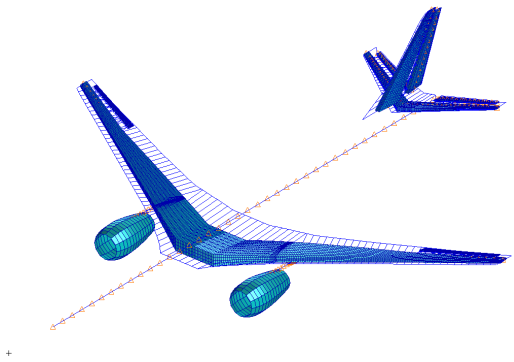

Figure 5 – FE model of the XRF1-DLR-C

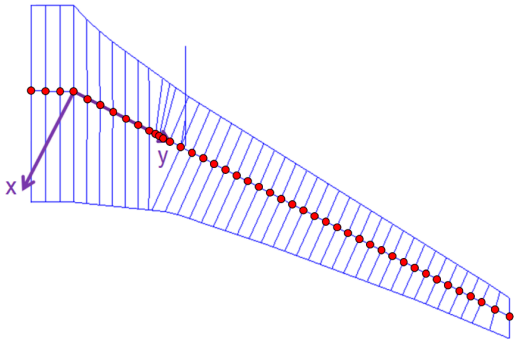

Figure 6 – Load reference axis nodes on the starboard wing, along with their local coordinate system

The FE model is then condensed onto load reference axis (LRA) nodes to reduce the number of degrees of freedom and due to the fact that only the global stiffness and mass properties are of interest in the loads analysis. The red dots in Figure 6 indicate the LRA nodes on the wing, along with their local coordinate system.

In the lifting surfaces, the loads are commonly evaluated in the LRA system. In the ideal case, the LRA lies in the elastic axis (e.g. of the wing box) and draw a straight line from the root to the tip. The aim of the first aspect is to be able to qualitatively estimate the wing deformation based on the loads without running simulations, and the aim of the second aspect is to have as few LRA coordinate systems as possible to simplify the load plots. As a compromise, the LRA nodes are roughly located in the center points of the ribs.

The structural and mass properties of the XRF1-DLR-C are an outcome of an iterative design process based on the MONA process [10]. The main part of the design process comprises a loads analysis and a subsequent structural optimization. In the loads analysis part, a total of 216 quasi-steady maneuver cases, 756 dynamic gust cases and one quasi-steady landing case are simulated with the Vortex Lattice Method (VLM), s. Table 2. V_C/M_C, V_A and V_D are the design cruise speed/Mach number, the design maneuver speed and the design dive speed, respectively. The operating empty mass is denoted as OEM and the maximum take-off mass as MTOM.

Table 2 – Overview of the maneuver and gust load cases of the clean high-speed configuration

Load condition	**Maneuver**	**Gust**
Mass configurations	**9** (OEM to MTOM, with center of gravity positions between 18 % and 40 % of mean aerodynamic chord)	**9**
Altitudes	**3** (0 m to 8300 m) The latter is where V_C coincides with M_C	**3**
Maneuvers per altitude	**8**, comprising: • 2.5 g pull-ups at V_A and V_D • -1.0 g push-downs at V_A and V_C • accelerated rolls at V_A (0 g and 1.67 g) • accelerated yaw at V_A • accelerated pitch-up at V_A	
Gusts per altitude		**28**, comprising: • 7 gust gradients (9-107 m) at V_C • 2 configurations (airbrake-in and airbrake-out) • 2 gust directions (upward and downward)
Total	**9*3*8 = 216**	**9*3*28 = 756**

Following the simulations, the loads are post-processed to extract the ones that are relevant for structural sizing and to carry out the structural optimization. Remark: the flight load cases taken for the optimization are high-speed cases with retracted high-lift devices only. The steps with the loads analysis and structural optimization are repeated until the change in the wing box mass between two cycles is below 0.2 %. For the pull-up maneuver cases, maneuver load alleviation (MLA) employing the ailerons and the three outermost spoilers is implemented. For dynamic pressures up to V_C, the MLA deflection is 20 deg for the ailerons and the spoilers, and above that, the deflection is set inversely proportional to the dynamic pressure. Further details regarding the modeling, loads and optimization can be found in [9].

2.4 Load cases

To estimate relevant high-lift load conditions, various load cases were derived based on EASA's CS-25 [5]. It includes requirements for certification of large aeroplanes and stipulates several conditions a device must withstand. Considering a rigid aircraft geometry and a conservatively chosen most forward center of gravity for static CFD calculations, the load cases investigated here vary in deflection of high-lift devices, aircraft mass and its distribution in the wing, airspeed, load factor and gust conditions. Take-off configuration 1+F, 2 and 3 are evaluated with MTOM, maximum zero fuel mass (MZFM) and OEM. Landing configuration Full was evaluated with maximum landing mass (MLM), MZFM and OEM as well as MTOM at 1.5 g as overload cases. The slow flight conditions are set at sea level which makes the airspeeds for the high-lift load cases solely equivalent airspeeds (EAS). The load cases cover stall speeds V_S, the take-off and landing reference speeds $V_{2,min}$ and V_{ref} and the flap design speed V_F. $V_{FE} < V_F$ represents the flaps extended speed as an upper limit during operation. $V_{F9} = V_F + 9\ kts$ is an upper limit at which the kinematics must be able to retract the high-lift devices (CS 25.697 (d) [5]). Despite the fact that the engine thrust may change the loading on wing and high-lift devices, it was neglected in this study, since in low speed condition, thrust in take-off may reduce the necessary lift force, thus reducing the wing load. During landing the engine is usually in flight idle. The impact on torsion on the wing box due to the engine position should already

be covered in the high-speed cases. Furthermore, the gust conditions were estimated considering aerodynamic characteristics of the aircraft configuration and superposition of gust velocity and rigid body motion of the aircraft response in an equation of motion. The aircraft elasticity (AMC 25.345(a) [5]) and flow dynamics during gusts were disregarded. The gusts to be analyzed for high-lift devices (CS 25.345(a)(2) and (b)(2) [5]) include a vertical gust from above, one from below and a horizontal head-on gust with an amplitude of 7.62 m/s and a gust gradient of 12.5 times reference chord length. All three gust types were analyzed for each configuration and their corresponding weight conditions representing 27 load conditions. Figure 7 shows exemplarily the effect of a gust from below with its gust velocity V_{gust}, the change of effective velocity at the aircraft ΔV_{eff} and the load factor n_z for configuration 3 at V_F for MTOM and OEM. While the gust imposes greater changes in effective airspeed and lower load factors on the configuration with MTOM, the lighter aircraft loading (OEM) shows smaller changes in effective airspeed and higher resulting load factors. Both, the effective airspeed affecting dynamic pressure and the load factor representing the acceleration, contribute to the overall loads and are summarized in a load function $n_z \cdot \left(\frac{V_{eff}}{V_F}\right)^2$. The maximum and minimum value of this function represent the load condition which is analyzed with static CFD calculation. For the gust from below the maximum value is 1.34 for the heavy aircraft and 1.54 for the light one. The gust from above causes a minimum load function value of 0.64 for MTOM and 0.24 OEM. The head-on gust as the third gust type, depicted in Figure 8 with different scale for ΔV_{eff}, induces greater changes in effective airspeed compared to the vertical gusts but weaker maximum load function values, which result in 1.28 and 1.25 for MTOM and OEM, respectively. The weak vertical motion of the aircraft compared to the relative high head-on velocities of the gust leave only minimal differences of effective velocity at the aircraft between MTOM and OEM.

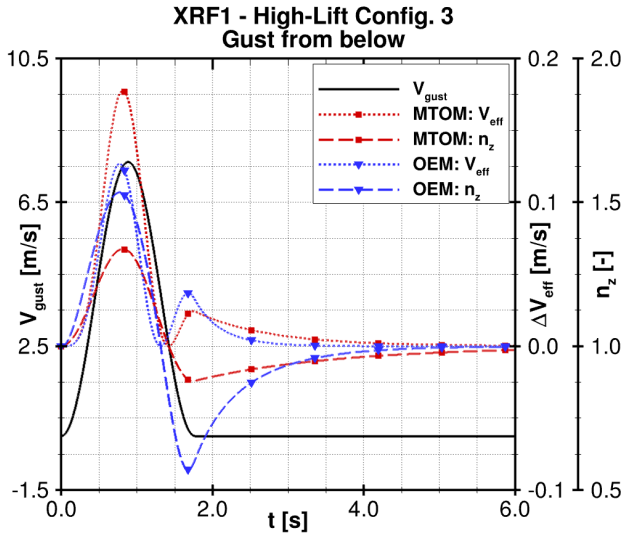

Figure 7 – Effect of gust from below on rigid body motion of XRF1 in configuration 3 with MTOM and OEM

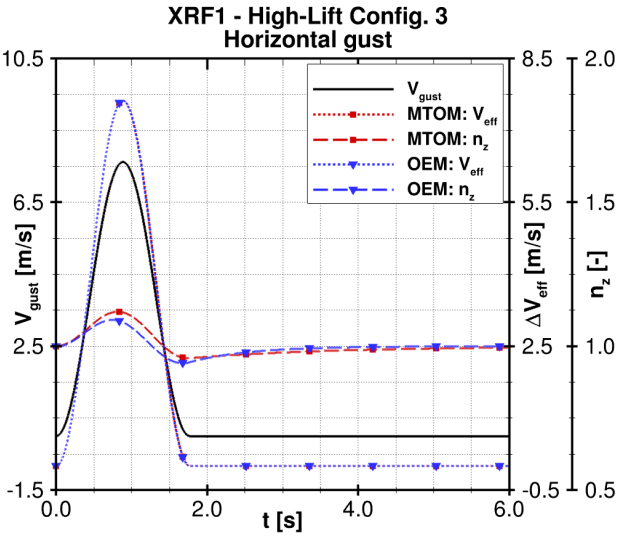

Figure 8 – Effect of horizontal head-on gust on rigid body motion of XRF1 in configuration 3 with MTOM and OEM

Considering the fact that some flow conditions are identical, 170 load cases were identified that are positioned at the edge of the flight envelope and inside in order to cover possible non-linearities, s. Table 3. Figure 9 depicts the estimated load cases in a load factor over equivalent airspeed plot for high-lift configurations 1+F. Every aircraft weight has its own "stall"-curve. During the CFD simulation, which will be described in the following section, different aerodynamic effects occurred, e.g. reduced maximum lift $C_{L,max}$ due to an increased Mach number. By that, an increase of the necessary stall speed for the 2 g load case was required. However, this was only the case for configuration 1+F with MTOM and MZFM. Figure 10 shows the calculated load cases plotted over the design lift curve to give an overview of the different combinations of airspeed and angle of attack.

Table 3 – Overview of the maneuver and gust load cases of the high-lift low-speed configurations

Load condition	Maneuver	**Gust**
Mass configurations	**3** • OEM, MZFM and MTOM for config. 1+F, 2, 3 • OEM, MZFM and MLM for config. Full	**3**
Center of gravity	**1**, most forward center of gravity (13 % of mean aerodynamic chord)	**1**
High-Lift configurations	**4**, comprising 1+F, 2, 3, Full	**4**
Airspeed / Load factor	**12** • V_S (load dependent), V_{FE}, V_F & 0 g, 1 g, 2 g • $V_{2,min}$ (Take-off) / V_{ref} (Landing) & 0 g, 1 g • V_{F9} & 1 g	**1**, at $V_{eff,gust}$ & $n_{z,gust}$
Gust types		**3** • Vertical gust from below • Vertical gust from above • Horizontal head-on gust
Additional	**-16**, redundant 0 g cases (OEM & MZFM, V_{FE} & V_F, all config.) **3**, overload cases: config. Full, MTOM at 1.5 g **3**, approach: config. 3 with MLM at V_S	
Total	**3*4*12 - 16 + 3 + 3 = 134**	**3*4*3 = 36**

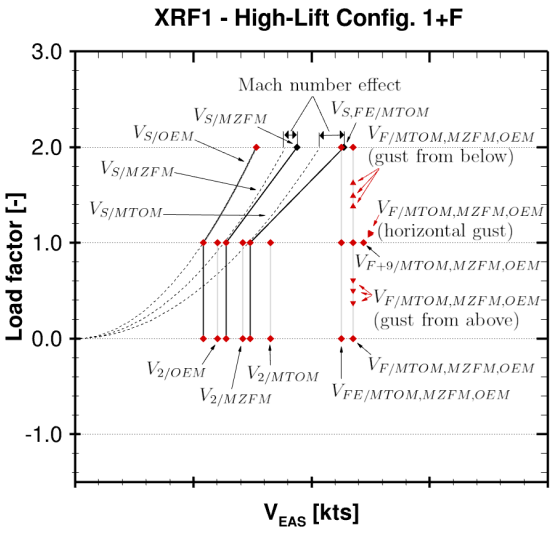

Figure 9 – Load cases of high-lift configuration 1+F to be certified

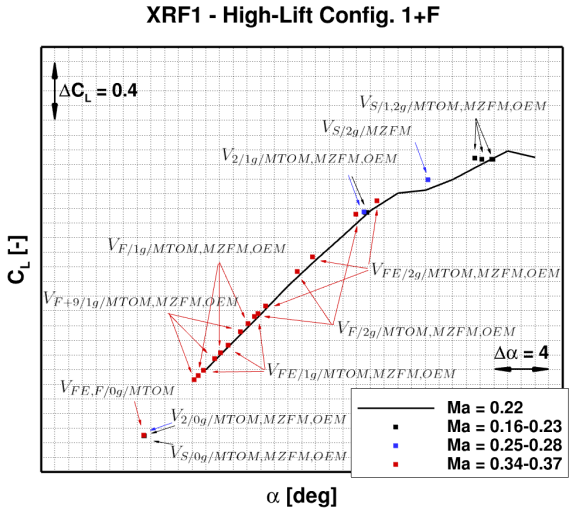

Figure 10 – Lift curve of high-lift configuration 1+F with calculated load cases and their conditions

3. Numerical Approach

To generate CFD field solutions for aerodynamic analysis the DLR-TAU [11] solver was used. It solves the three-dimensional compressible Reynolds-Averaged Navier-Stokes (RANS) equations on unstructured hybrid grids of finite volumes. Flux discretization is realized via a spatially second order

accurate central scheme with artifical matrix dissipation. The applied relaxation solver is an implicit Backward-Euler procedure with the lower-upper symmetric Gauss-Seidel (LUSGS) scheme. To accelerate the convergence, a multigrid method was applied and the turbulence was introduced with the Spalart-Allmaras negative model [12]. The solver and in memory data management was controlled with the python based FlowSimulator framework [13].
The flow field discretization of the half model was carried out with the SOLAR grid generator. This grid generator is able to reliably reproduce highly structured quad-dominant surface meshes on which hexahedra dominant boundary layers can be build up. Farfield refinement was done at the wing tip and neglected behind the wing due to the lack of an empennage. Regarding different Reynolds numbers a first cell height of $1 \cdot 10^{-6}$ m ensured a y^+ of maximum 0.5 for every load case. These resulted in a grid of around 120 Mio. points.
A grid convergence study based on Richardson Extrapolation [14] for configuration 3 indicates a Grid Convergence Index (GCI) of less than 1.4 % for lift and pitching moment coefficient and less than 0.1 % for the drag coefficient based on the grid used here and a coarser one. Further analysis of the outboard flap alone shows GCI values of around 0.5 % for the forces and 2.0 % for the moments around the X-, Y- and Z-axis. The surface solutions of both grids show good agreement and indicate asymptotic behavior, i.e. flow topology close to the extrapolated exact solution.
To ensure a flow field around the wing equal to one of a trimmed aircraft an iterative process was implemented. After a sufficient number of iteration steps, when satisfying convergence was reached, the untrimmed lift and pitch moment coefficient was used to calculate a virtual HTP downforce. This downforce then leads to a new target C_L which was aimed to by changing the angle of attack.

4. Data processing & Evaluation

4.1 Wing cut loads

The aerodynamic loads were distributed onto a structural model represented by the LRA with discrete nodes described in Section 2.3. This was realized by using an interpolation method based on finite interpolation elements (FIE) [15, 16]. The interpolation algorithm assigns the CFD grid points to a beam element between two nodes of the LRA by orthogonal projection and distributes its force and moment fractions to the right or left hand node. In a first run the aerodynamic force of each grid point was distributed onto its corresponding LRA-node assuming a force introduction given by the interpolation algorithm itself. In order to achieve a more realistic force introduction via slat and flap kinematics, a second cycle of the process was carried out. This time, the surface parts of each device were grouped and assigned manually to specific LRA-nodes. This node assignment is exemplarily illustrated by colors in Figure 11 for the flaps and trough-flow nacelle (TFN).
Subsequently, to obtain the structural cut loads, the aerodynamic loads are superposed with the inertial loads resulting from the acceleration (gravitational and centrifugal) of the respective load case. Figure 12 shows the shear forces F_z of an example load case. The first process cycle is named as continuous (cont.) and the second as discrete (discr.). The interpolated aerodynamic loads at each LRA-node are shown as a red graph with black symbols. Peaks are caused at nodes which concentrate a greater amount of forces, which are a combination of the number of CFD grid cells and their corresponding loads, e.g. nodes of the TFN between wingspan position η of 0.3 and 0.35. In contrast to that a higher concentration of LRA-nodes leads to shorter beam elements, which reduces the sum of forces at these nodes. This is the case between $\eta = 0.25$ and 0.3.
The continuous approach causes a relative smooth graph behavior in the outboard region due to the more uniform distributed LRA-nodes and load distribution. Three bumps of the graph represent the increased loads introduced by the outboard flap between $\eta = 0.45$ and 0.7. The intentional device-to-node assignment of the discrete approach lets the graph appear far more peaky. This in combination with the orthogonal projection causes an inboard shift of the peaks representing the forces of the outboard flap. The continuous approach lets the tracks appear farther outboard than they are.
The black lines show the resulting cut loads including the inertial loads of the corresponding aircraft loading. Minor absolute differences between the continuous and discrete approach are apparent close to the outboard flap tracks and major differences are visible close to the TFN pylon and out-

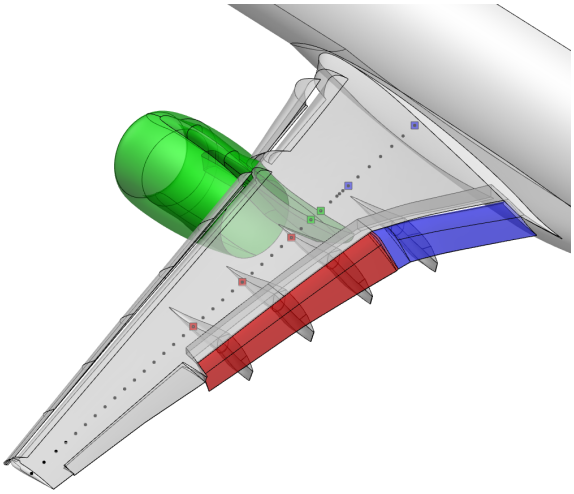

Figure 11 – LRA-node assignment for different wing parts (e.g. TFN, flaps)

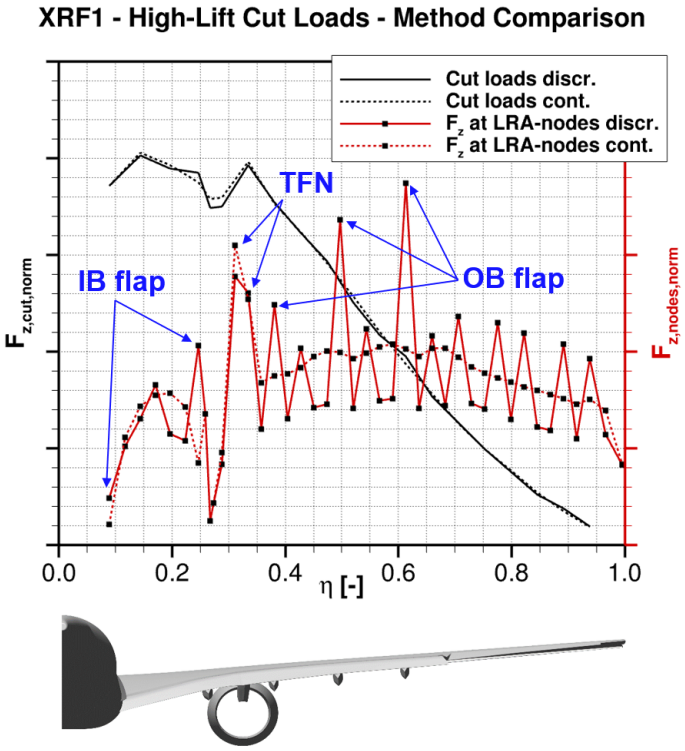

Figure 12 – Comparison of continuous and discrete force distribution on structural model

board flap track of the inboard flap. The relative differences to the continuous approach are estimated to ± 2.7 % at the inboard region and -4.7 % to $+7.1$ % at the outboard region. The outboard flap track region shows relative differences of -2.3 % to $+4.2$ %. In the following, the second cycle approach, e.i. the discrete method, is used for further comparisons. The spanwise distributed support points of the cut load graph correspond to every second LRA-node.

Figures 13 and 14 show shear forces F_z and bending moments M_x of all maneuver load cases analyzed. The cut load data is normalized to the maximum value of F_z and M_x at each LRA-node. The highest loads here are given for high aircraft weights and high load factor. The lack of relieving fuel masses of the MZFM load cases raises the shear forces at wing root at $\eta = 0.09$ above the loads imposed by the higher total weight cases MTOM and MLM. All of these load conditions are characterized by very different angles of attack and airspeeds (s. Figure 10). The wing bending moments are dominated by the MTOM and MLM load cases at 2 g.

Minimum loads of F_z and M_x are produced by those load cases with a load factor of 0 g. The drop of shear forces below zero at the wingtip is dominated by high-lift configuration 1+F with MTOM; here higher airspeeds generate even lower shear forces.

The torsional moments M_y depicted in Figure 15 are normalized to the most positive value at each LRA-node. They are most positive for high weights and high load factors, too. Only the most negative values are not represented by the 0 g cases anymore. The negative peak of the graph comes from the combination of the mainly up-pitching TFN and down-pitching inboard flap (s. Figure 12). A look at Figure 16 reveals a set of maneuver cases which are connected with high airspeeds: $V_{EAS} \geq V_{FE}$. This set is additionally split into high (MTOM, MLM) and low wing mass (MZFM, OEM). The combination of high airspeed and low wing mass gives the critical load cases representing the negative limit of the torsional moment. Further on, a separation into groups of high-lift configuration of these load cases reveals that a greater deflection of the high-lift device results in greater torsional moments. The greater lever of the higher flap setting leads to greater nose down moments which are only partly compensated by the increased slat deflection.

Figures 17 to 19 introduce the gust load cases. Shear forces and bending moments of these cases are mainly inside the maneuver load envelope. Only three cases of a vertical gust from above push

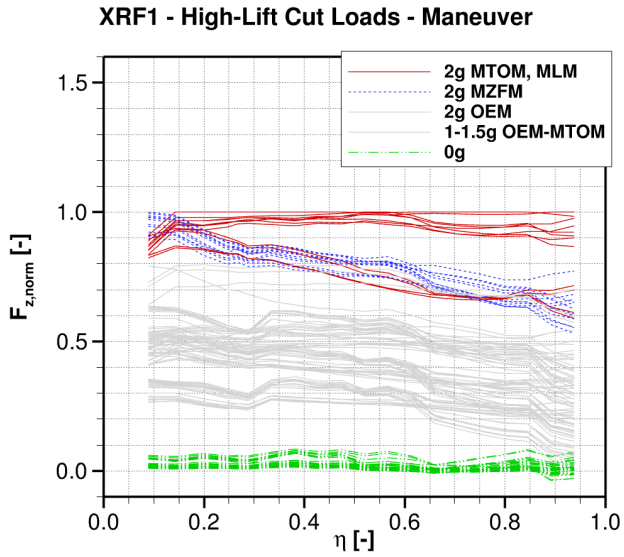

Figure 13 – Cut loads: normalized shear forces F_z of maneuver cases

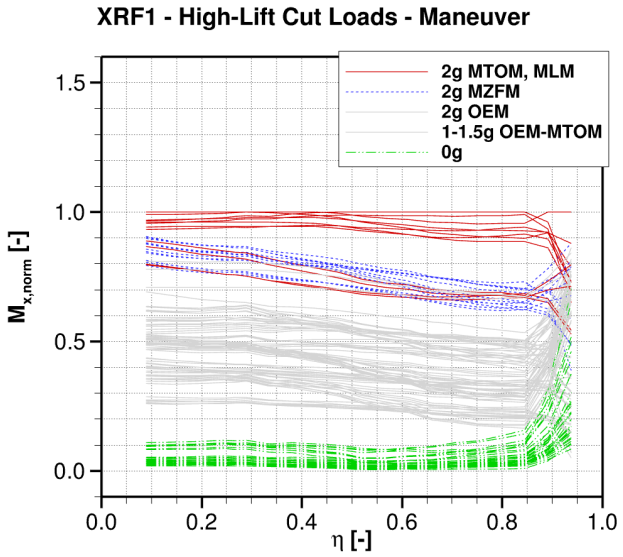

Figure 14 – Cut loads: normalized bending moments M_x of maneuver cases

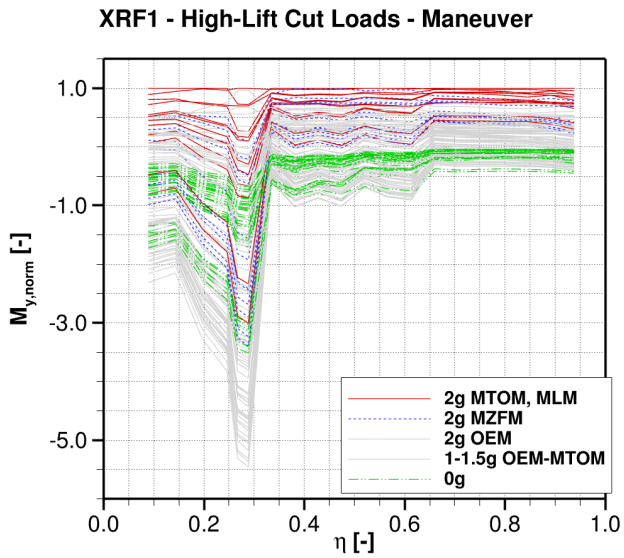

Figure 15 – Cut loads: normalized torsional moments M_y of maneuver cases

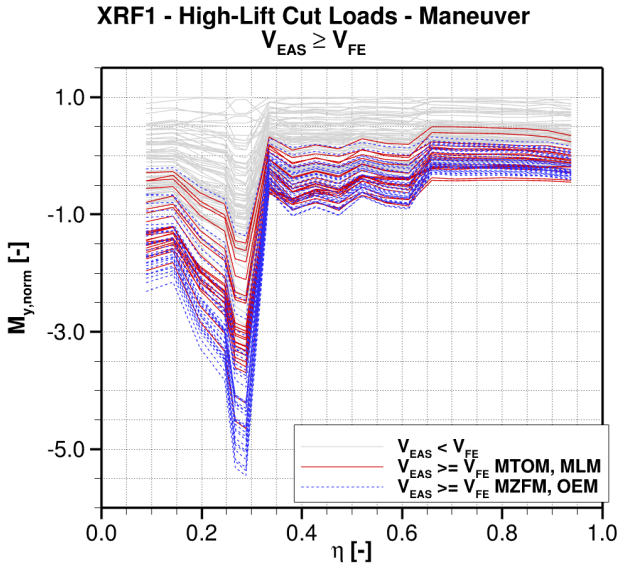

Figure 16 – Cut loads: normalized torsional moments M_y of high airspeeds $V_{EAS} \geq V_{FE}$

the shear forces close to the wingtip below zero. This is the case for configuration Full with MZFM and MLM and for configuration 3 with MZFM.

The torsional moments of the gust load cases impact the lower limit. This is estimated to an increase in magnitude of the negative torsional moment of 6 % at $\eta = 0.29$ compared to the maneuver loads. A breakdown of parameters of the gust load cases leads to the same hierarchy like mentioned for the maneuver cases. Low wing mass and greater high-lift device deflection create the strongest negative torsional moments. The hierarchy coming from gust type parameter is depicted in Figure 20. The velocity increase due to the horizontal gust confirms the prior experienced effect of airspeed on the torsional moments in Figure 16.

In the following the high-lift load cases are compared to the cruise load cases mentioned in Table 2. The depicted gust and maneuver envelopes of the cruise load cases as red, solid and blue, short-dashed line in Figure 21 and 22 reflect the maximum values reached at each spanwise position. (The lower envelope of the cruise flight load cases is not visible.) Hence, F_z, M_x and M_y are not necessarily correlated. It should be noted that the cruise load cases are calculated with an elastic geometry.

The applied MLA, as described in Section 2.3, reduces the maneuver loads below the gust loads. The former are usually higher for heavier aircrafts. This makes the gust loads mainly responsible for maximum shear forces and bending moments in cruise flight. The shear forces at root and midboard

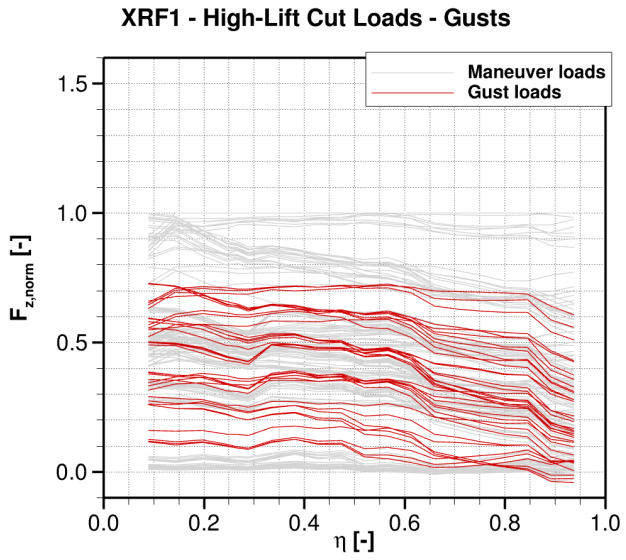

Figure 17 – Cut loads: normalized shear forces F_z with gust cases

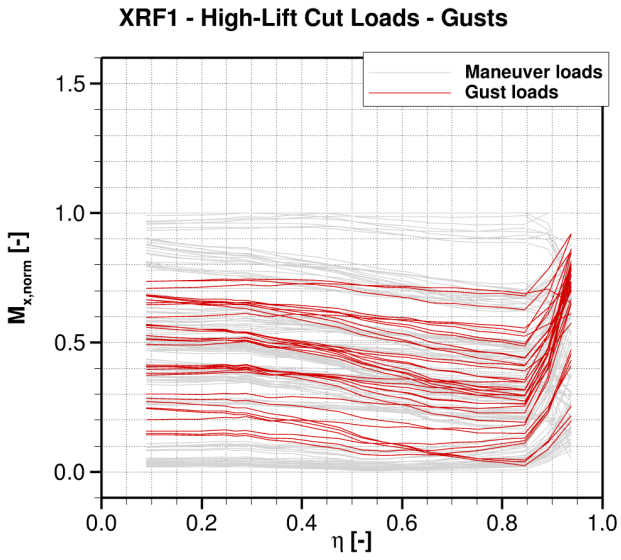

Figure 18 – Cut loads: normalized bending moments M_x with gust cases

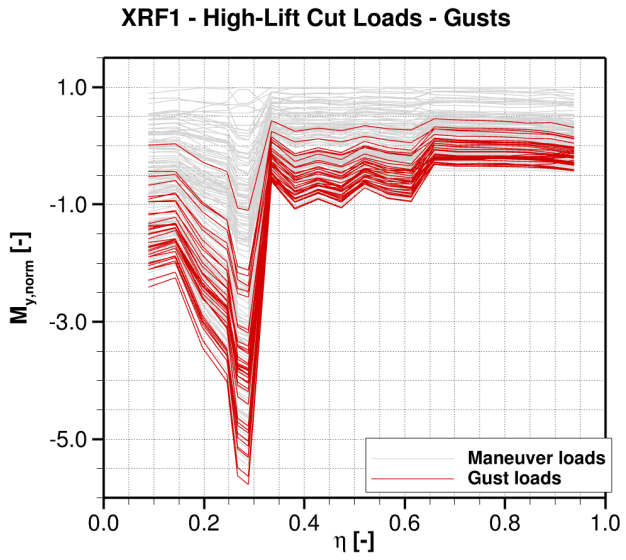

Figure 19 – Cut loads: normalized torsional moments M_y with gust cases

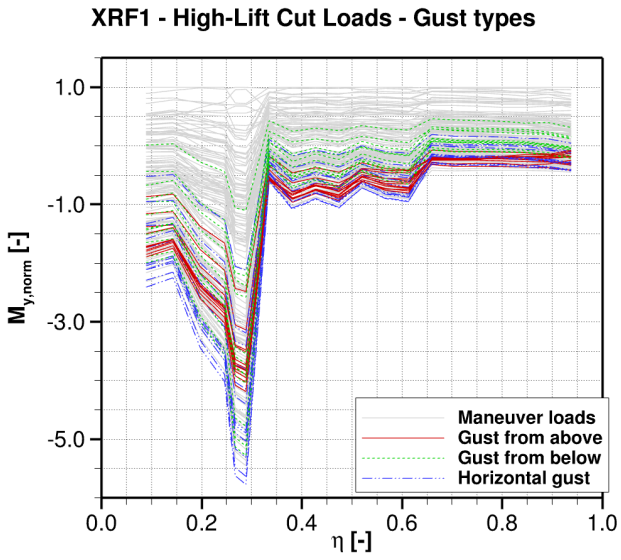

Figure 20 – Cut loads: normalized torsional moments M_y of gust types

at $\eta = 0.33$ are exceeded by the high-lift loads by 4 % and 22 %, respectively. High-lift shear forces at wing tip reach only 85 % compard to gust loads in cruise flight. The M_x load limit at root lies 10 % above the cruise flight gust loads but the difference decreases to the wingtip. The wing tip bending moments imposed by the cruise flight gusts are three times higher than the maximum high-lift loads. This emphasizes the inboard shift of the high-lift load distribution by the slats and flaps.
Comparing the torsional moments in Figure 23, no high-lift load case becomes critical. The maximum M_y in cruise flight was generated by a pull-up maneuver of $+2.5$ g at V_A.
Regarding the fact that the high-lift load cases were calculated with a rigid aircraft geometry the relieving effect of elasticity is of interest. This is addressed by calculating a cruise flight load case with a non-elastic geometry at 1 g, MTOM and V_C. In Figure 21 to 23 this can be taken from the black,

long-dashed and dash-double-dotted lines. The shear force reduction can be estimated to 10 % at root and 44 % at wing tip. The bending moments are reduced by 20 % and 35 % at root and wing tip, respectively. The effect on the torsional moments is small but visible.

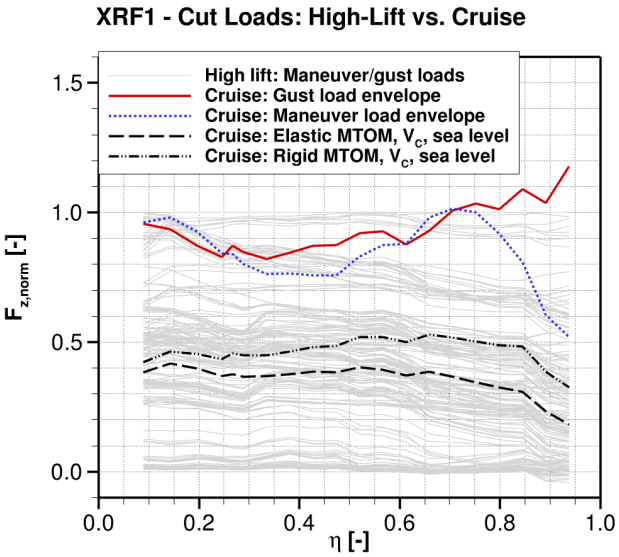

Figure 21 – Cut loads: normalized shear forces F_z of high-lift loads and cruise load envelope

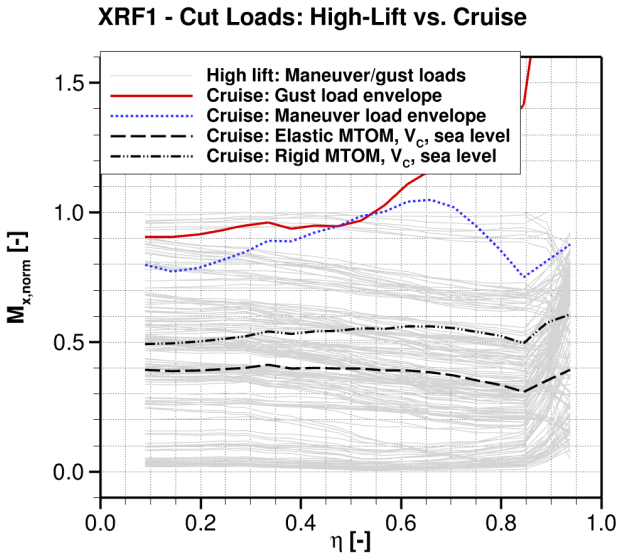

Figure 22 – Cut loads: normalized bending moments M_x of high-lift loads and cruise load envelope

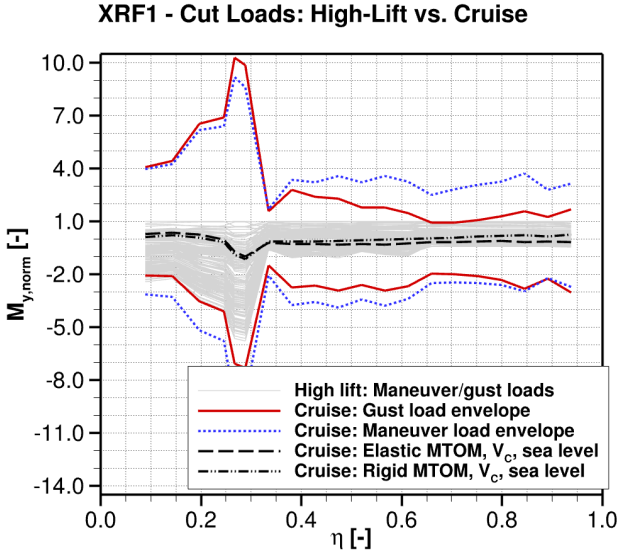

Figure 23 – Cut loads: normalized torsional moments M_y of high-lift loads and cruise load envelope

In contrast to the cruise geometry, the high-lift geometry leads to an inboard shift of the wing load distribution that reduces the bending moment and thus the deformation. Overall elasticity may bring down the high-lift loads below the cruise flight envelope but the margin between cruise flight loads and high-lift loads are small in this comparison.

4.2 High-lift device loads

An in-house tool named AeroForce [17] gives the possibility to evaluate the CFD surface solutions and to estimate forces and moments by integrating pressure and viscous forces on specified surfaces,

e.g. slats and flaps. After creating reference systems, the normal and tangential forces F_n and F_t as well as the pitching moments M_y on each high-lift device are extracted. The used coordinate systems are shown in Figure 24 and positioned at the inboard edge of the corresponding high-lift device. The moments are related to the leading point of the airfoil at $\eta = 0.5$ of each device. Figure 25 depicts a set of resultant force vectors on the inboard slat of configuration 3 to emphasize the various load conditions a high-lift device must withstand. Different load cases cause forces that strain the slat and flap kinematics in various ways. Normal forces create stresses mainly normal to the tracks while tangential forces need to be withstanded by the actuators extending and retracting the devices. To build up a hierarchy to identify critical load cases, normal and tangential forces were normalized to the maximum positive value of all maneuver load cases. The negative pitching moment related to the leading edge was normalized to the most negative value of all maneuver load cases. The normalization is done for each high-lift device separately.

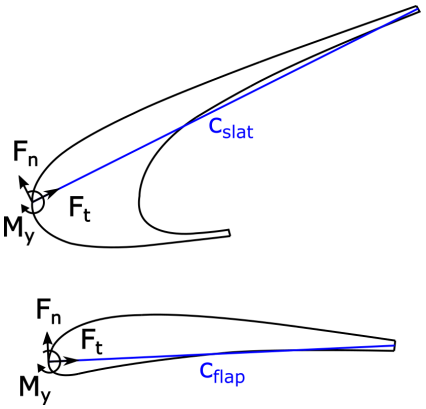

Figure 24 – Coordinate systems of slats and flaps

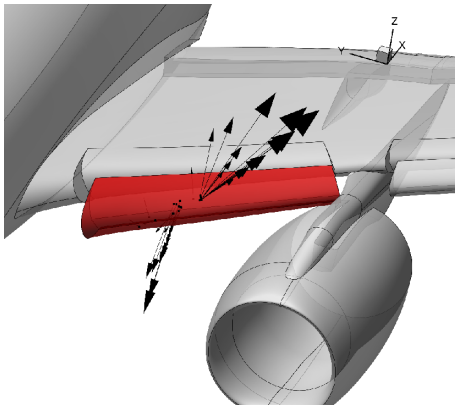

Figure 25 – Resultant force vectors on inboard slat for different load cases of configuration 3

In Figure 26 and 27 the seven left columns represent the slat devices and the two columns on the right hand side the inboard and outboard flap. The hierarchy of all maneuver load cases already found in Section 4.1 can be transferred to the normal forces and pitching moments of the slats. High aircraft mass and load factor generate the highest loads on these devices. However, the maximum flap loads are generated by other load cases. Again the 0 g load cases represent the load cases imposing minimum loads on slats and flaps. To identify the critical load cases for the flaps a parameter

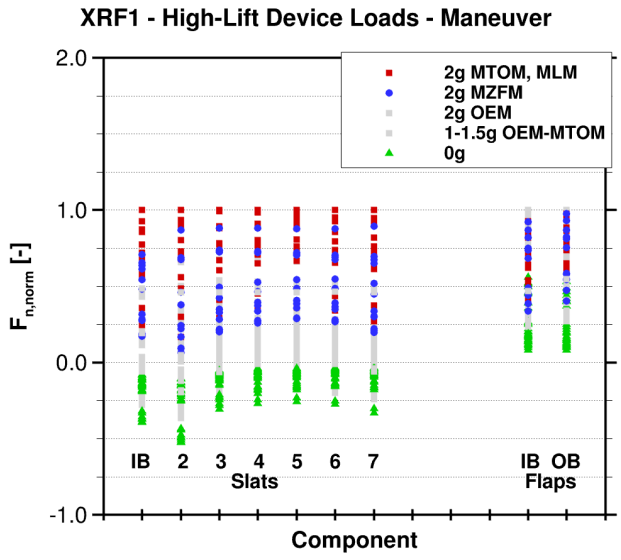

Figure 26 – High-lift device loads: normalized normal forces F_z of maneuver cases

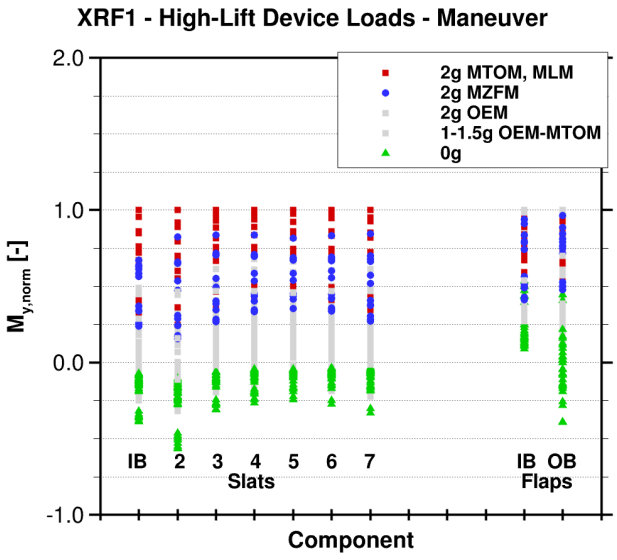

Figure 27 – High-lift device loads: normalized normal forces M_y of maneuver cases

breakdown is necessary. From Figure 28 and 29 it can be taken that high airspeeds $V_{EAS} \geq V_F$ and flap deflection are responsible for the highest normal forces and pitching moments. Less aircraft loading and lower load factors reduce the generated loads. Two load cases exist where the outboard flap shows lower pitching moment for configuration Full (orange, diamond symbols in Figure 29). They are characterized by low aircraft mass OEM which leads to low α compared to higher aircraft weights and in this situation to a strong flap separation. The tangential forces of the outboard flap are plotted

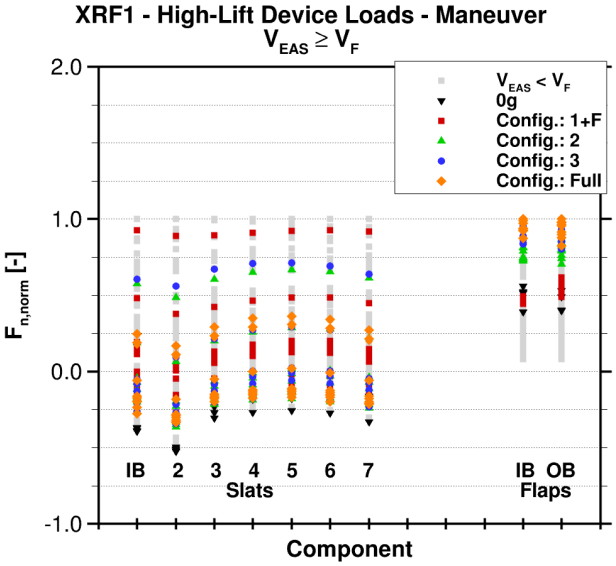

Figure 28 – High-lift device loads: normalized normal forces F_n of maneuver at $V_{EAS} \geq V_F$

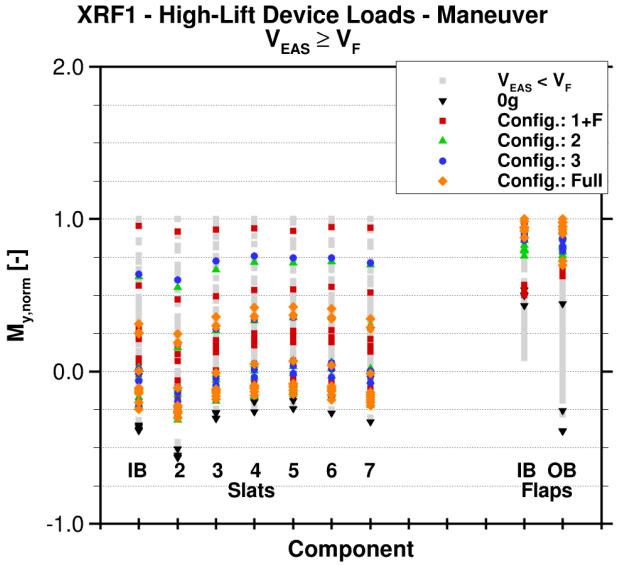

Figure 29 – High-lift device loads: normalized normal forces M_y of maneuver at $V_{EAS} \geq V_F$

in Figure 30 over the angle of attack. In addition, several groups of airspeed and the 0 g load cases are marked Arrows show the increase of loads for configuration 1+F and the decrease to negative values for configuration 2, 3 and Full with increasing V_{EAS}. Figure 31 shows the tangential forces over V_{EAS}. The necessary airspeed increase due to the effect of the Mach number mentioned in Section 3. is visible for configuration 1+F at V_{FE} in the top right corner. The last three columns of symbols represent V_{FE}, V_F and V_{F9} for each high-lift setting.

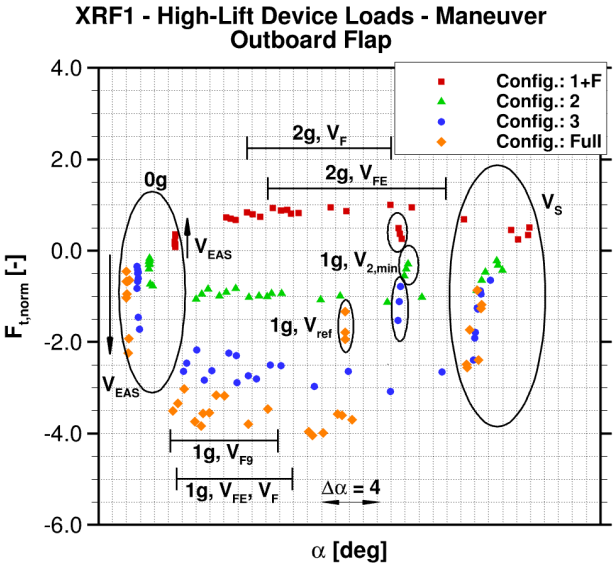

Figure 30 – High-lift device loads: normalized tangential forces F_t over α of outboard flap

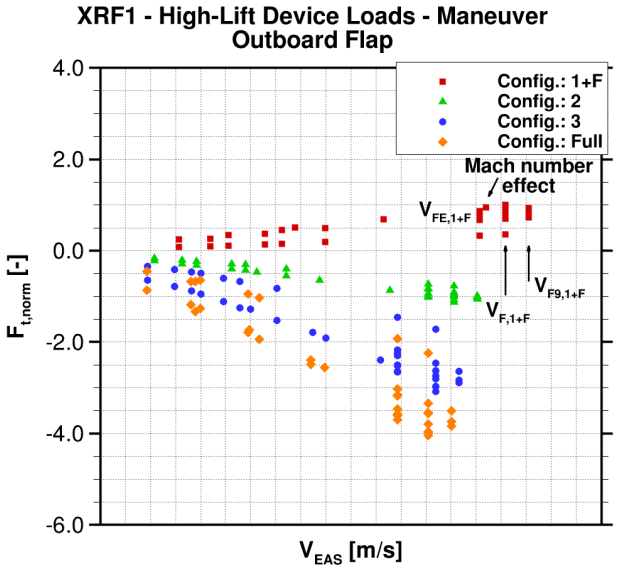

Figure 31 – High-lift device loads: normalized tangential forces F_t over V_{EAS} of outboard flap

The complex dependency of α and V_{EAS} creates a tub out of the symbols for each high-lift con-

figuration. Configuration 1+F represents the positive limit with moderate angles of attack and high airspeeds. With more flap deflection the course of the graph flips upside down and an increase of airspeed reduces the loads to negative values. The inboard flap shows a similar behavior with only minor differences. The tub shape is not fully pronounced and the minimum tangential forces are shifted to higher V_{EAS} and lower α.
To estimate the critical tangential forces for the slats an analysis of the variation over angle of attack is necessary. It is shown in Figure 32 for the inboard slat. Again, several marks represent groups of airspeed and the decreasing tangential forces due to inreasing airspeed for the 0 g cases. While the pattern of the symbols mainly stays the same for all slats, different maximum and minimum values can be identified for the inboard slat, slat 2 and slat 3 to 7. The maximum forces on all slats are

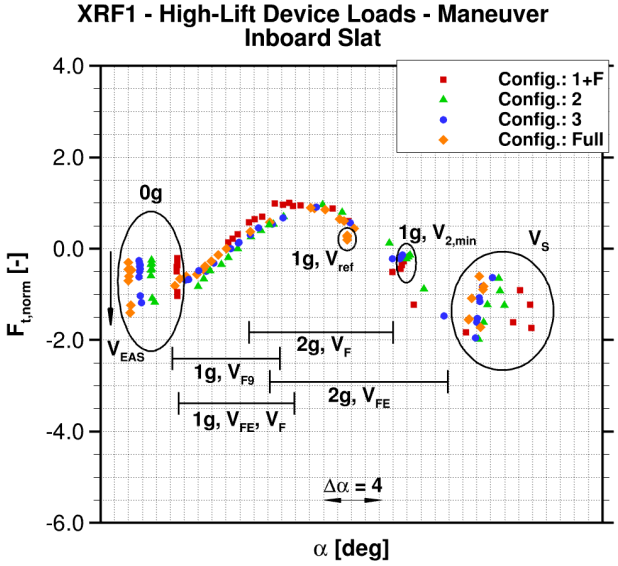

Figure 32 – High-lift device loads: normalized tangential forces F_t over α of inboard slat

imposed by load cases at moderate angle of attack at high airspeeds of V_{FE}, V_F and V_{F9}. The critical values are those imposed by load cases of configuration 1+F with a 15 deg deflection. The minimum tangential forces are caused by different high-lift settings. All of them are characterized by high load factors (2 g) and high angle of attack at stall speed. As an exception, the minimum forces at slat 2 are generated by 0 g load cases with high airspeed V_F.
In Figure 33 and 34 the gust load conditions named by their gust type are introduced for the normal forces and pitching moments. No effect on the slat envelope can be identified. Regarding the flaps the higher velocities introduced by the horizontal gust raise the upper limit of the normal forces by 7 % and 4 % for the inboard flap and outboard flap, respectively. The pitching moment is increased for both flaps by around 7 %.
The tangential forces on the outboard flap due to the gusts are shown in Figure 35 over α. While the maximum forces due to horizontal gust stay shortly below the maneuver limits the lower envelope is widened by 1 % for the outboard flap and more than 6 % for the inboard flap. Increasing aircraft mass increases flap loads depending on configuration, i.e. higher loads for configuration 1+F and stronger negative loads for configuration Full.
The effect of the horizontal gusts on the tangential forces on inboard slat and slat 3 to 7 is estimated to up to 9 % and is exemplarily depicted in Figure 36 for slat 6. A new maximum value for slat 2 is set by a gust from below by more than 1 %.

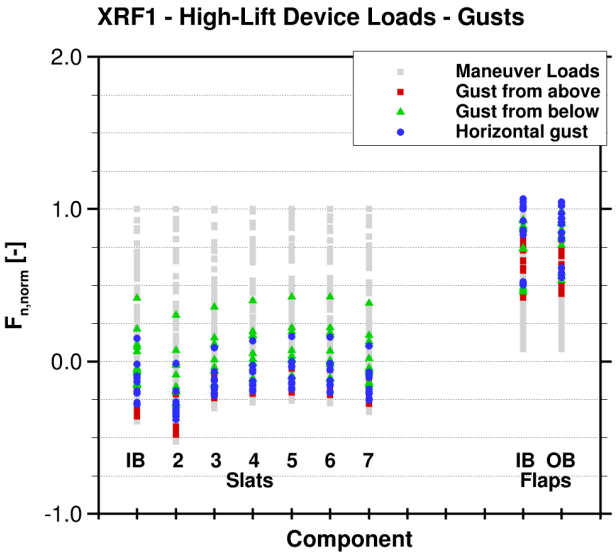

Figure 33 – High-lift device loads: normalized normal forces F_n of gust load cases

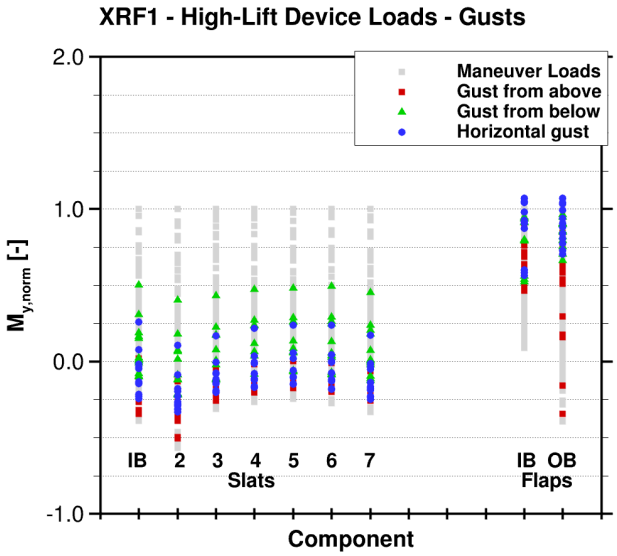

Figure 34 – High-lift device loads: normalized pitching moments M_y of gust load cases

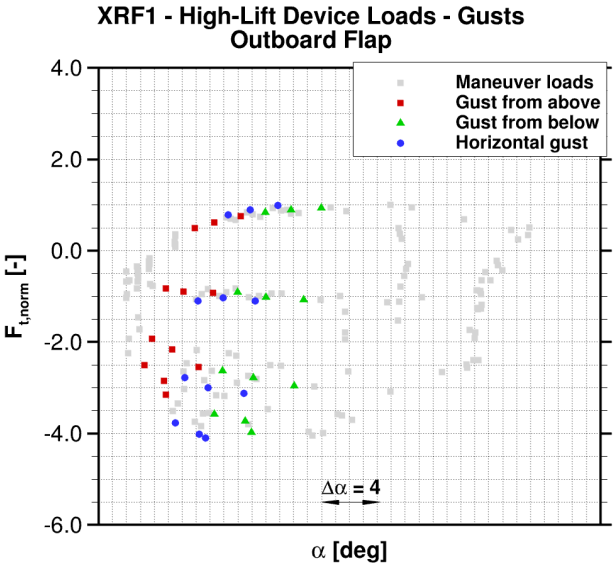

Figure 35 – High-lift device loads: normalized tangential forces F_t over α of outboard flap

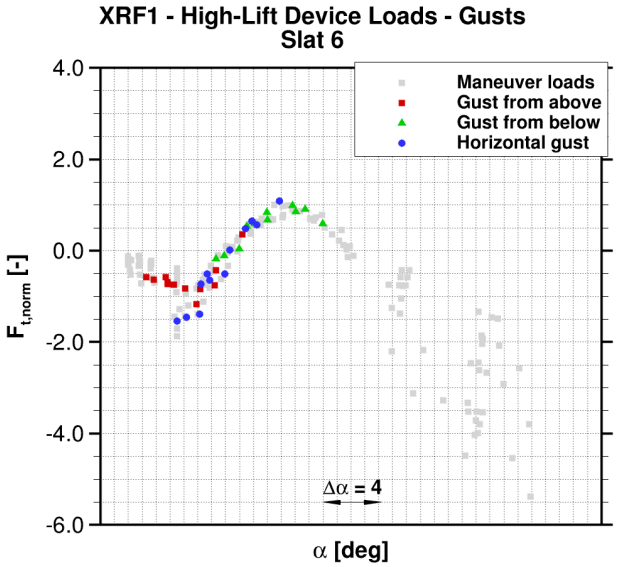

Figure 36 – High-lift device loads: normalized tangential forces F_t over α of slat 6

5. Conclusions

After the presentation of the XRF1 with its newly designed high-lift devices and the structural model, 170 maneuver and gust load cases and their different parameters were introduced. The CFD calculations with the DLR TAU-solver provided aerodynamic forces which were post processed to cut loads on wing and forces and moments on high-lift devices. While the analysis of the high-lift device loads provide a load hierarchy for flaps and slats, the wing cut loads offer the possibility to establish a wing load hierarchy.

The critical shear forces and bending moments are mainly driven by maneuver load cases with high weight and high load factor whereas torsional moments are dominated by load cases with reduced wing mass at high airspeed. Here, higher deflection angles of the high-lift devices lead to greater loads. Load cases with gusts, especially horizontal gusts, generate even more negative torsional moments.

The load comparison of high-lift and clean configuration reveals that the alleviated cruise flight loads are exceeded to some extend by the non-alleviated high-lift loads for this aircraft and structural model.

The lack of elasticity during high-lift CFD calculations makes it possible that the high-lift loads will be reduced below those of the alleviated cruise flight loads but they are relatively close to each other and the inboard shift of the wing load distribution in high-lift conditions diminishes this effect. So if the high-lift loads are still dominant for wing sizing after further investigations, it will most likely be necessary to apply load alleviation in high-lift to take full advantage of the weight reduction due to load alleviation technologies.
The hierarchy of high-lift device loads shows that the normal forces and pitching moments are dominated either by high weight and high load factor load cases for the slats or by load cases with high airspeed and high deflection for the flaps. The flap loads are only exceeded during horizontal gust cases. Lower limits for slats and flaps come from 0 g load cases.
The tangential forces require a deeper analysis of angle of attack, airspeed and high-lift device setting. Maximum positive loads on flaps and slats are driven by high speed cases at moderate angle of attack with configuration 1+F. The most negative tangential forces on the flaps are reached by the same conditions but at the highest deflection angle in configuration Full. The lower limit for the slats is either imposed by high angle of attack at V_S for inboard slat and slat 3-7 or by the 0 g load cases for slat 2. Again the horizontal gusts increase maximum positive loads to some extend.

6. Acknowledgement

The authors thank the Federal Ministry for Economic Affairs and Climate Action (Bundesministerium für Wirtschaft und Klimaschutz - BMWK) for the funding as part of LuFo V-3 in the project In-Fly-Tec/APLAUS. Similarly, the authors thank Airbus for providing the XRF1 testcase as a mechanism for demonstration of the approaches presented in this paper. Special acknowledgement goes to Jochen Wild for the high-lift design, his advice and support, and Stefan Melber-Wilkending for generating the CFD meshes. In addition, acknowledgement goes to the Virtual Product House (VPH) in Bremen for supporting further CFD analysis (grid convergence study).

7. Contact Author Email Address

For technical questions please contact sven.puelm@dlr.de

8. Copyright Statement

References

[1] Xu J, Kroo I. Aircraft design with active load alleviation and natural laminar flow. *Journal of Aircraft*, Vol. 51, No. 5, pp. 1532-1545, 2014.

[2] Binder S, Wildschek A, De Breuker R. The interaction between active aeroelastic control and structural tailoring in aeroservoelastic wing design. *Aerospace Science and Technology*, Vol. 110, 2021, 106516, ISSN 1270-9638, https://doi.org/10.1016/j.ast.2021.106516.

[3] Handojo V. *Contribution to load alleviation in aircraft pre-design and its influence on structural mass and fatigue*. DLR Research Report, DLR-FB-2020-47, Dissertation, TU Berlin, 2021, https://elib.dlr.de/139558/.

[4] Bertram O. Nekon - *Neue Entwurfsmethoden zukünftiger Steuerflächenkonzepte (im LuFo V.2 Con.Move-Verbundprojekt)*. Project report, DLR-IB-FT-BS-2020-232, 2020, https://elib.dlr.de/139686/.

[5] European Union Aviation Safety Agency. CS25 - Certification specifications and acceptable means of compliance for large aeroplanes. Amendment 24, 2020.

[6] Pattinson J, Herring M. High fidelity simulation of wing loads with an active Winglet Control Surface. *IFASD 2013 - International Forum on Aeroelasticity and Structrual Dynamics*, Bristol, United Kingdom, 2013.

[7] Bramsiepe KRB, Handojo V, Meddaikar MY, Schulze M, Klimmek T. Loads and structural optimisation process for composite long range transport aircraft configuration. *AIAA Aviation Forum*, Atlanta, Georgia, 2018, https://doi.org/10.2514/6.2018-3572.

[8] Görtz S, et al. Overview of collaborative multi-Fidelity multidisciplinary design optimization activities in the DLR project VicToria. *AIAA Aviation Forum*, Virtual Event, 2020, https://doi.org/10.2514/6.2020-3167.

[9] Handojo V, Klimmek T, Streit T. Loads analysis and structural optimization of a long-range transport configuration with hybrid laminar flow control. *33rd Congress of the International Council of the Aeronautical Sciences*, Stockholm, Sweden, 2022 (tbp)

[10] Klimmek T. Parametric set-up of a structural model for FERMAT configuration for aeroelastic and loads analysis. *ASD Journal*, Vol. 3, No. 2, pp 31–49, 2014.

[11] Langer S, Schwöppe A, Kroll N. The DLR flow solver TAU - status and recent algorithmic developments. *AIAA SciTech - 52nd Aerospace Sciences Meeting*, National Harbor, MD, USA, 2014, https://doi.org/10.2514/6.2014-0080.

[12] Allmaras S R, Johnson F T, Spalart P R. Modifications and clarifications for the implementation of the spalart-allmaras turbulence model. *Seventh International Conference on Computational Fluid Dynamics (ICCFD7)*, Big Island, Hawaii, ICCFD7-1902, 2012.

[13] Reimer L. The FlowSimulator - A software framework for CFD-related multidisciplinary simulations. *European NAFEMS Conference*, Munich, Germany, 2015.

[14] Roache P J. *Verification and Validation in Computational Science and Engineering*. Hermosa Publishers, Albuquerque, NM, USA, 1998.

[15] Beckert A. Coupling fluid (CFD) and structural (FE) models using finite interpolation elements. *Aerospace, Science and Technology*, Vol. 4, No. 1, pp 13-22, 2000.

[16] Braun C. *Ein modulares Verfahren für die numerische aeroelastische Analyse von Luftfahrzeugen*. Dissertation, RWTH Aachen, 2008.

[17] Wild J. *AeroForce - thrust/drag bookkeeping and aerodynamic force breakdown over components update v 0.6.8*. DLR Internal Report, DLR-IB-AS-BS-2018-51, 2018.